

This is an Open Access document downloaded from ORCA, Cardiff University's institutional repository:<https://orca.cardiff.ac.uk/id/eprint/115633/>

This is the author's version of a work that was submitted to / accepted for publication.

Citation for final published version:

Yang, Ming, Liu, Yue, Zhu, Hanxing , Zhang, Fan, Fan, Tongxiang and Zhang, Di 2018. Influences of interfaces on dynamic recrystallization and texture evolution during hot rolling of graphene nanoribbon/Cu composites. *Metallurgical and Materials Transactions A* 49 (12) , pp. 6401-6415. 10.1007/s11661-018-4921-8

Publishers page: <http://dx.doi.org/10.1007/s11661-018-4921-8>

Please note:

Changes made as a result of publishing processes such as copy-editing, formatting and page numbers may not be reflected in this version. For the definitive version of this publication, please refer to the published source. You are advised to consult the publisher's version if you wish to cite this paper.

This version is being made available in accordance with publisher policies. See <http://orca.cf.ac.uk/policies.html> for usage policies. Copyright and moral rights for publications made available in ORCA are retained by the copyright holders.



Influences of Interfaces on dynamic recrystallization and texture evolution during hot rolling of graphene nanoribbon/Cu composite

Ming Yang¹, Yue Liu¹, Hanxing Zhu², Fan Zhang¹, Tongxiang Fan^{1}, Di Zhang¹*

¹State Key Laboratory of Metal Matrix Composites, Shanghai Jiao Tong University, 800

Dongchuan Road, Shanghai 200240, P. R. China

²School of Engineering, Cardiff University, Cardiff CF24 3AA, UK

*Corresponding author. Tel: +86-21-54747779. E-mail: txfan@sjtu.edu.cn (Tongxiang Fan)

Abstract The incorporation of carbon nanofillers into bulk metal matrices has stimulated tremendous interest to translate their intriguing properties from nanoscale to the macroscopic world. However, the influences of such rigid hetero-interfaces on the dynamic recrystallization (DRX) process and texture evolution of the composite system remain an open issue. Here we report interface-dominated DRX and texture evolution phenomena in a graphene nanoribbon (GNR)-reinforced Cu matrix composite during hot-rolling. The GNR/Cu interfaces contribute to the atypical recrystallization-type and brass-type textures developed in composites within 0.5 vol.% and 3 vol.% GNRs, respectively, deviating from the normal Cu-type texture found in their pure Cu counterpart. We prove that the hetero-interfaces may change the texture evolution of the Cu matrix from four aspects including retarding dislocation cross slip, generating geometrically necessary dislocations, promoting the DRX process, and activating non-octahedral slip. This is corroborated by visco-plastic self-consistent simulations, which

well reproduce the texture development in all samples by considering the interface-dislocation interaction, GNR-driven DRX nucleation, and the activation of non-octahedral slip. This study suggests the possibility of manipulating the microstructure, texture, and mechanical properties of traditional metallic materials through the design of heterophase interfaces.

1. Introduction

The texture development in metals, alloys and composites containing hetero-phase interfaces during deformation has long been a general interest of both material science and industrial applications [1-3]. Most industrial alloys contain a matrix phase and dispersed second-phase particles (SPPs). The introduction of particle or fiber reinforcement into metal matrix composites (MMCs) through *ex-situ* blending methods provides further freedom for designing the fraction, distribution, alignment, size, and geometry of the SPPs. A wide variety of studies have proven that the inclusion of SPPs creates additional interfaces within the matrix, which may highly impact the deformation behavior of the matrix material [1]. The recrystallization (RX) behavior, crystallographic texture evolution, and associated mechanical properties of the investigated alloys [4-7] or composites [8] are substantially influenced by the complex interfacial interaction between the matrix material and the SPPs during the common (thermo-)mechanical processing.

Recently, the incorporation of low-dimensional (from 0D to 2D) nanofillers into bulk metal matrices has attracted tremendous interest to translate their intriguing properties from nanoscale to the macroscopic world [9-11]. Graphene has been regarded as one of the most promising reinforcement for MMCs due to its peculiar 2D, single-atom-thick nanostructure, and excellent intrinsic physicochemical properties. Graphene nanosheets have shown great

capacity for improving the strength, stiffness, toughness, and thermostability of pure metals. To date most studies focus on improving the reinforcing efficiency through uniformly dispersing graphene into the metal matrix [12-14], improving the interfacial bonding between graphene and the metal phase [15], and explicating the reinforcement role and strengthening mechanisms of graphene [16-18]. Several thermo-mechanical processing steps (*e.g.*, hot-rolling [12, 17] and hot-extruding [14]) are usually needed to produce a final metal-graphene composite product. However, very little is known about the plastic deformation regime, dynamic RX (**DRX**), and texture evolution of such metal-graphene systems during thermo-mechanical processing, and their dependence on the hetero-phase interfaces in the composite remains an open issue.

Graphene features 2D planer nanostructure and ultra-large specific surface area, giving rise to a large interfacial contact area in the relevant MMCs. Of interest here is how the presence of such high densities of immiscible interfaces can potentially alter the relative activities of slip or twinning in the matrix phases and in turn, texture evolution with strain, compared to those in their pure metal counterparts. These effects have been widely documented in multi-phase composites like Cu-Nb layered composites produced by accumulated roll bonding [19] and Cu-Ag eutectic-layered alloy [20, 21]. Moreover, the special geometry and nanoscale effect of graphene, which are distinctly different from the micrometer-sized, granular or rod-like SPP in traditional industrial alloys, may trigger new phenomena in terms of shear banding, slipping and twinning modes, DRX behavior, and texture evolution in graphene-reinforced MMCs.

Herein, we investigate the effects of metal-graphene hetero-interfaces on the DRX and texture evolution during hot-rolling deformation using a graphene nanoribbon (**GNR**)-

reinforced Cu matrix composite system. GNRs are novel quasi-1D carbonaceous nanomaterials combining elegantly the properties of 2D graphene and 1D carbon nanotubes (CNTs). GNRs feature high levels of strength, flexibility, stiffness and surface area, flat geometry and large aspect ratio and have shown great capacity to enhance the overall physico-mechanical properties of pure metals [12]. Cu is selected as a model matrix because it has a relatively simple deformation mode, and thus it is easy to isolate the role of the GNR/Cu interfaces (GCIs). We demonstrate that the GCIs contribute to the atypical textures developed in GNR-reinforced Cu-matrix composites (GNRs/Cu), as compared to the traditional Cu-type texture formed in their pure Cu counterpart. As illustrated by micro-area electron back-scattered diffraction (EBSD), transmission electron microscope (TEM), high-resolution TEM (HRTEM), and Kernel average misorientation (KAM) analyses, the GCIs may change the texture evolution of the Cu matrix from four aspects: i) retarding dislocation cross slip; ii) generating geometrically necessary dislocations (GNDs); iii) promoting the DRX process; and iv) activating non-octahedral slip. We further carry out visco-plastic self-consistent (VPSC) polycrystal simulations to identify and interpret the roles of GNRs and GCIs in altering the slip mode, deformation mechanism, and DRX behavior of the Cu matrix.

2. Experimental

2.1 Material preparation and processing

GNRs/Cu were prepared by a powder metallurgy approach consisting of solution-based hetero-aggregation of Cu/GNR powder mixtures [22], rapid densification of the hybrid powders by spark plasma sintering (SPS), and hot-rolling. The hybrid powders were consolidated by SPS (HPD-25, FCT Systeme GmbH) at 600 °C for 5 min with an applied

pressure of 50 MPa. The as-SPSed samples were first cut into slabs of 28mm × 12mm × 3.5mm and then annealed at 800 °C for 30min. A fast, multi-pass rolling process was conducted on a Φ100 mm two-high mill with final true strains of 0.36–1.94. The samples were rapidly quenched in water to preserve the microstructure in its as-deformed state. The raw materials, synthesis of GNRs, and preparation process were detailed in our previous studies [12, 18, 23]. GNRs/Cu containing 0.5 vol.%, 1 vol.%, and 3 vol.% GNRs were prepared by adjusting the amount of GNR additive and were denoted as 0.5GNR/Cu, 1GNR/Cu, and 3GNR/Cu, respectively.

2.2 Characterization

Samples for X-ray diffraction (**XRD**) and EBSD texture measurements were prepared by standard mounting, grinding, and polishing. The final two polishing steps consisted of vibratory polishing (VibroMet 2, Buehler) with 0.05 μm colloidal alumina and 0.05 μm colloidal silica suspensions. The bulk texture was characterized by the Schulz reflection method, using an X-ray texture goniometer with Cu K_{α} radiation (D8 Advance, Bruker), operating at 30 kV and 25 mA. Data collection was performed with sample rotation increments of 5° and a maximum sample tilt of 80°. The acquisition time was 3 s and the sample oscillation was 6 mm. Four incomplete pole figures from (111), (200), (220), and (311) peaks were collected on a mid-thickness section parallel to the RD-TD (**RD**, rolling direction; **TD**, transverse direction) plane, and they were corrected for background defocusing and used to determine the orientation distribution function (**ODF**) with the WIMV algorithm, using a MTEX software available as a MATLAB[®] toolbox.

EBSD was performed on a field-emission scanning electron microscope (**SEM**, Nova

NanoSEM 230, FEI) fitted with an AZTec HKL Max EBSD detector at an accelerating voltage of 20 kV. EBSD data were collected from the cross-sectional samples (*i.e.* RD-ND plane; **ND**, normal direction). The scanning step size for EBSD was 0.02–0.5 μm according to the size of the scanning area. The inverse polar figure (**IPF**) maps, ODF figures, polar figures (**PFs**), texture intensity, fractions of different texture components (with a 15° deviation from their ideal orientations), and KAM maps were obtained from post-treatments of the EBSD orientation data using the HKL Channel-5 software. KAM maps were constructed by calculating the misorientation angle of every measurement point up to its third nearest [24]. The microstructure of the as-rolled samples was characterized using a field-emission SEM (S-4800, HITACHI). TEM and HRTEM (JEM 2100F, JEOL) operating at 200 KV were used to obtain the information on the dislocation configuration, nanostructure, and interfaces of the samples. TEM samples were prepared by standard polishing and ion milling (Gatan PIPS, Model 691, Oxford).

3. Results and discussion

3.1 Microstructure and texture evolution

Fig. 1a-h show the evolution of the distribution of GNRs in the Cu matrix as a function of the rolling reduction. Primarily the three-step preparation method including wet-fusing assembly of Cu/GNR hybrid powders, fast sintering and hot-rolling [12, 18] enables well-embedded, uniformly distributed, and individually dispersed GNRs in the Cu matrix. In addition, lengthwise rotation of GNRs occurs along with the plastic flow and lattice rotation of the Cu matrix, leading to a realignment of GNRs parallel to the RD. Specifically, GNRs transform from distributing randomly in the as-SPSed composite (**Fig. 1a**), to gradually rotate

to the RD with the increasing of rolling deformation (**Fig. 1b-c**), and finally to be perfectly parallel to the RD (**Fig. 1d**). This is corroborated by a statistic of the ξ (*i.e.*, the angle between the GNR axis and the RD) values, which shows a very narrow distribution of orientation angle ξ between 0–10° at a true strain (ϵ) of 1.94 (**Fig. 1e-h**). The dynamic rotation of GNRs during deformation impose further complexity to assess the effect of GNR inclusion on the DRX behavior and texture evolution of GNRs/Cu. Nonetheless, it is notable that no obvious distorted or rotated zone is detected in GNRs/Cu (**Fig. 1i-j**) [4-6, 25]. The atomic-level thickness of GNRs contributes to a much thinner GNR-affected zone (**GAZ**) in GNRs/Cu than the obvious particle affected deformation zone (**PAZ**) observed in industrial alloys containing large constituent SPPs.

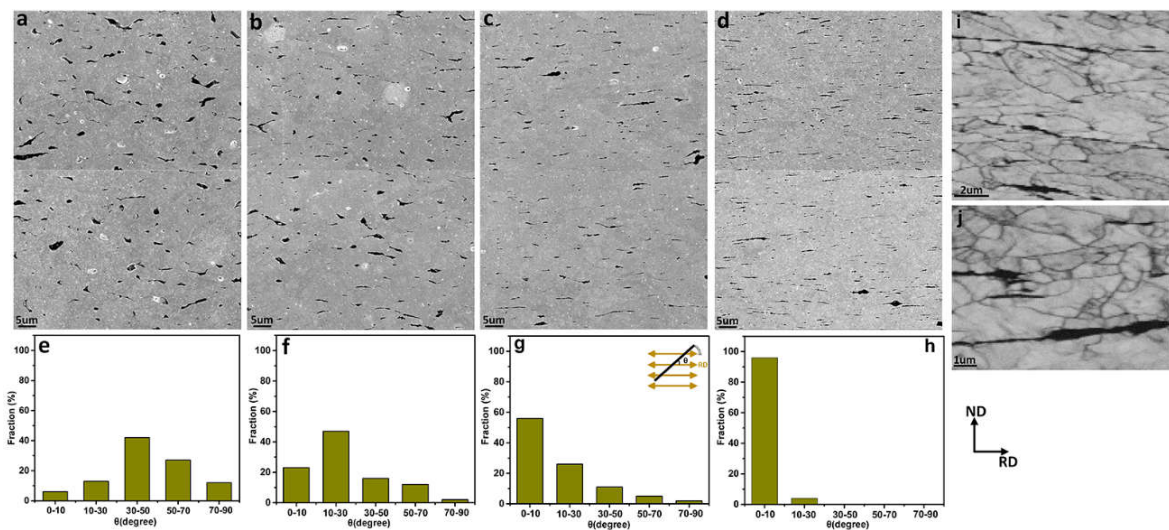


Fig. 1. (a-d) Alignments of GNRs in 3GNR/Cu at $\epsilon = 0$ (as-sintered), 0.36, 0.69, and 1.94, respectively. (e-h) The distributions of the orientation angle (ξ) corresponding to (a-d). (i-j) EBSD band contrast maps showing no obvious distorted or rotated zone around GNRs.

The developments of macro- and micro-textures in pure Cu and GNRs/Cu are examined by XRD and EBSD. The ODF maps retrieved from XRD measurement (**Fig. 2**) are, in general, in

agreement with those from EBSD data, which can verify the accuracy and reliability of crystallographic texture obtained from EBSD analysis. Nevertheless, the micro-texture, which is derived from the EBSD mapping implemented in the middle thickness position, is detected to be slightly different from the macro- one. This is ascribed to the texture gradient frequently observed in the through-thickness direction of rolled sheets.

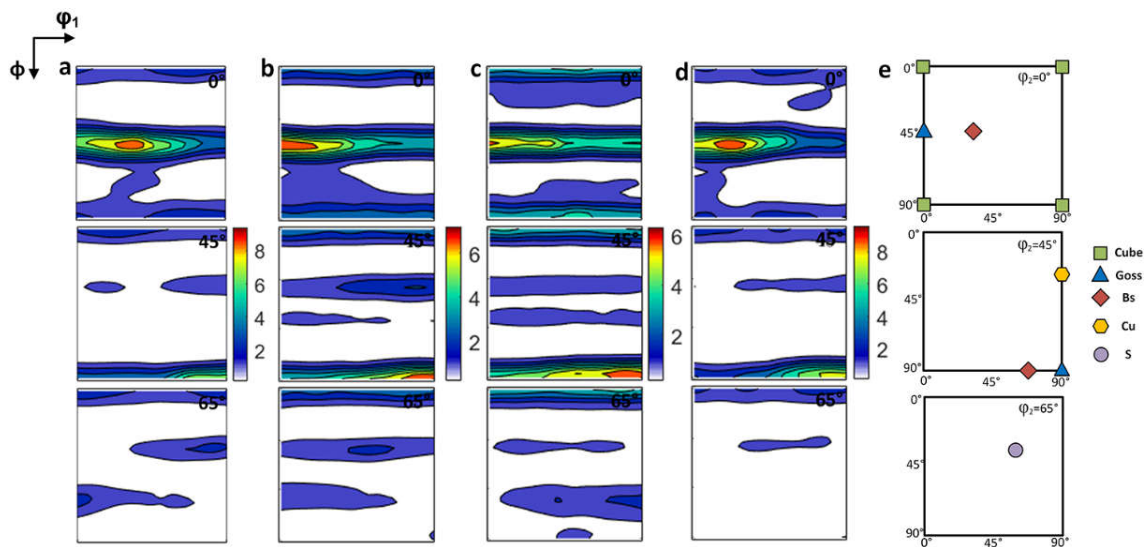


Fig. 2. (a-d) ODF figures obtained from XRD incomplete PFs. (e) A schematic representation of the important texture components in FCC materials, showing ODF sections of $\phi_2 = 0^\circ$, 45° , and 65° .

It is well documented that face-centered cubic (FCC) metals may, depending on material parameters (*e.g.*, stacking fault energy, **SFE**) and rolling paths, develop two different types of rolling textures [3, 26]. The Cu-type texture represents the deformation texture of metals with medium to high SFEs (*e.g.* 89 mJ m^{-2} for Cu) produced by conventional rolling processes [4, 5]. The so-called β -fiber, which consists basically of a tube in orientation space including as major components the orientations $(123)\langle 634 \rangle$ (S) and $(112)\langle 111 \rangle$ (Cu), together with a less

significant (110)<112> (**Bs**) component, characterizes the Cu-type texture. In contrast, the brass-type texture developed in highly alloyed metals with low SFE (*e.g.* Ag and 70:30 brass) features a dominance of Bs orientation and a less important (110)<001> (**Goss**) component [20, 27].

EBSD measurements indicate that the texture of the as-annealed, undeformed samples are essentially random (**Fig. S1**). According to the typical PFs (**Fig. 3**) and ODF maps (**Fig. 4a-d**) obtained from the XRD and EBSD measurements, the main characteristics of the texture developed in different samples are presented in Figure 3.

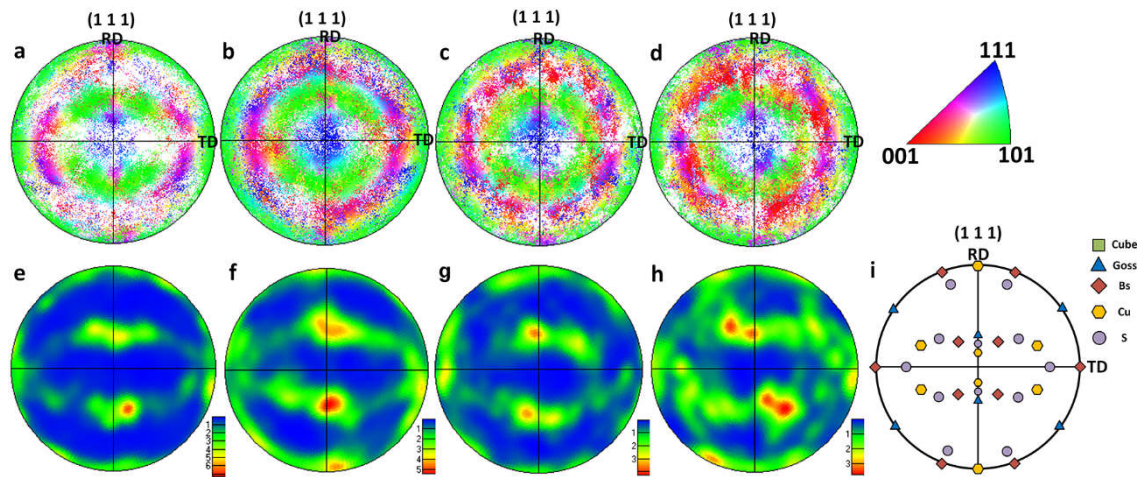


Fig. 3. (a-d) (111) PFs of pure Cu, 0.5GNR/Cu, 1GNR/Cu, and 3GNR/Cu, respectively. (e-h) (111) PFs derived from the orientation data corresponding to (a-d), respectively. (i) (111) PF showing the important texture components.

As expected, the rolling texture of pure Cu developed at $\epsilon = 1.94$ is basically composed of a standard β -fiber. The volume fractions of the major texture components in the pure Cu are: 29% Cu, 26% S and 12.9% Bs, which is a typical proportion for a Cu-type texture (**Fig. 4e**) [28]. With an inclusion of 0.5 vol.% GNRs, an obviously increased strength of Goss orientation is observed with the expense of the β -fiber (Cu, S, and Bs) components. When the GNR fraction

is increased to 1 vol.%, a strong Bs component reappears; the Cu and S components become weaker; and the intensity of Goss orientation is diminished as compared to that in 0.5GNR/Cu.

At a GNR fraction of 3 vol.%, the Goss orientation nearly disappears, and a predominant Bs component is detected with very weak Cu and S components remaining. The volume fractions of the major texture components in 3GNR/Cu are: 7.2% Cu, 11.4% S and 23.3% Bs, which is similar to a brass-type texture (Fig. 4e).

The overall texture intensity decreases sharply with the GNR fraction increasing, as shown in Fig. 4f. This can be correlated to the stimulating effect of GNRs on the dynamic recovery and DRX processes and will be detailed in Section 3.3.

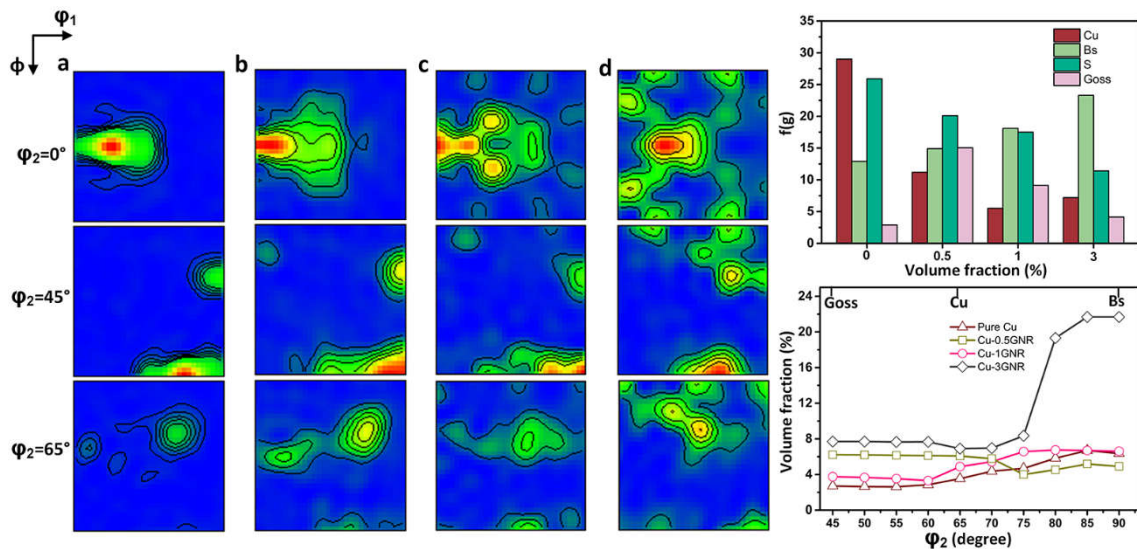


Fig. 4. (a-d) ODF images retrieved from the EBSD data of pure Cu, 0.5GNR/Cu, 1GNR/Cu, and 3GNR/Cu, respectively. (e) Volume fractions of the main texture components (Cu, Bs, S, and Goss) as a function of GNR fraction. (f) Texture intensities along the β -fiber of pure Cu and GNRs/Cu. **Characters e and f should be present in the above figures.**

3.2 Role of the GNR/Cu interface

The results in **Figs. 2-4** are surprising mainly for three reasons as follows: i) The observed texture development of GNRs/Cu appears to deviate remarkably from the Cu-type rolling texture; ii) With the GNR additive increasing, a dominant Goss component appears and then disappears; iii) While the SFE is kept constant, an approximate brass-type texture is developed in 3GNR/Cu.

Primarily all the samples are processed under the same applied strain path (*e.g.* annealing temperature, number of pass, and rolling reduction per pass), thereby the deviation of textures in GNRs/Cu from the expected one can only be attributed to the inclusion of GNRs and GCIs. Depending on the hot-rolling conditions, the hot band texture of FCC metals is dominated by deformation (*e.g.*, β -fiber; and α -fiber, $\langle 110 \rangle // ND$) or RX components (*e.g.*, Goss; **P**, $(110)\langle 332 \rangle$; and **Cube**, $(100)\langle 001 \rangle$) components or a combination of both [4]. Primarily, the texture evolution of FCC materials in hot-rolling is determined by the cross slip, twinnability, and competition between dislocation storage and oriented nucleation [29, 30]. Therefore, the introduction of GNRs and GCIs may impact the texture evolution from the following three aspects:

i) GNRs drastically interact with the dislocations at the interfacial sites in terms of dislocation initiation, propagation, motion, and annihilation, as proven by both experimental observations [12, 16, 17] and molecular dynamic simulations [31]. The manner of GCI-dislocation interaction greatly impacts the composite texture response. Firstly, the rigid interfacial areas may serve as high-capacity sinks for pinning down and thereby accumulating dislocations, especially as the specific interface area is as large as $3.48 \times 10^7 \text{ m}^2 \text{ m}^{-3}$ and the

inter-particle spacing is as narrow as $< 1 \mu\text{m}$ (Fig. 1d) in this study. Secondly, there are two ways that an interface can supply a lattice dislocation, either by emitting of a new loop *via* a stress concentration or by splitting (dissociating) a preexisting misfit dislocation into a lattice dislocation and a residual [31, 32]. Thirdly, GNDs are initiated at the GCIs due to the deformation incompatibility along with the mismatches of coefficients of thermal expansion (CTE) and elastic moduli [33].

ii) When the volume fraction of GCIs is sufficiently high, the interfaces may strongly retard the normal cross slip of dislocations and thereby activate non-octahedral slip in addition to the conventional (111)<110> slip system in FCC materials. For example, when interact with a GNR layer, it is possible for a single perfect dislocation with $\bar{b} = \frac{1}{2} < 0\bar{1}\bar{1} >$ gliding on the (11 $\bar{1}$) close-packed slip plane to spontaneously dissociate into two Shockley partials of lower energies defined as $\bar{b}_1 = \frac{1}{6} < \bar{1}\bar{1}2 >$ and $\bar{b}_2 = \frac{1}{6} < 1\bar{2}\bar{1} >$ [31].

iii) Like the particle stimulated nucleation effect of SPPs in traditional alloys, the inclusion of GNRs can provide additional nucleation sites, which accelerates discontinuous RX nucleation of the Cu matrix. Especially, the GNR-affected zone (**GAZ**) with high strain inhomogeneity is energetically favored as preferential RX sites. It has been documented that the β -fiber texture is retained during continuous RX processes, whereas discontinuous RX processes account for β -fiber rotation towards α - (*e.g.*, P, Bs, and Goss) and θ -fiber (Cube and (100)<011>) textures [4]. Therefore, the presence of GCIs can promote the formation of RX texture component.

3.3 GNR-stimulated DRX

First we attempt to clarify the relationship between the GCIs, DRX process, and final texture

development. The presence of non-deformable particles in commercially produced precipitation-containing alloys (*e.g.*, Fe [6] and Al alloys [34]) triggers additional strain hardening and heterogeneities in rolled materials due to the gradients of deformation proportional to the inter-particle spacing [5]. In the course of deformation, a special zone (*i.e.*, PAZ) is developed around such non-deformable SPPs, which is characterized by a high local strain and a high misorientation gradient [5]. During hot-rolling, the first recrystallized nuclei appear in the vicinity of the particle inclusions and this phenomenon refers to the well-known RX mechanism of particle stimulated nucleation, whereas the particle-free matrix exhibits the conventional rolling texture (β -fiber). Similarly, larger accumulated strains in the GAZ result in larger local driving force for RX. Firstly, GNRs modify the deformation structure in terms of stored energy, grain misorientation, and heterogeneity sites, which may significantly change the subsequent RX process. Secondly, GNRs may accelerate nucleation of RX, influence the orientations, and pin the growth of recrystallized grains [1].

EBSD map (**Fig. 5a**) shows that the as-rolled pure Cu have elongated, laminated or spindle-like grains, and almost no DRX grain is generated around the coarse, deformed grains. In contrast, some fine equiaxed grains, which are deemed to be recrystallized grains, are formed in the very vicinity of the GNRs (**Fig. 5b-c**). Deformed, recovered, and recrystallized components qualitatively estimated from the EBSD data indicate that the extents of dynamic recovery and DRX are enhanced linearly with the GNR fraction (**Fig. 5d-e**). This is supported by the much increased fraction of high-angle grain boundaries (**HAGBs**) in GNRs/Cu compared to that in pure Cu (**Fig. 5f**) [35, 36].

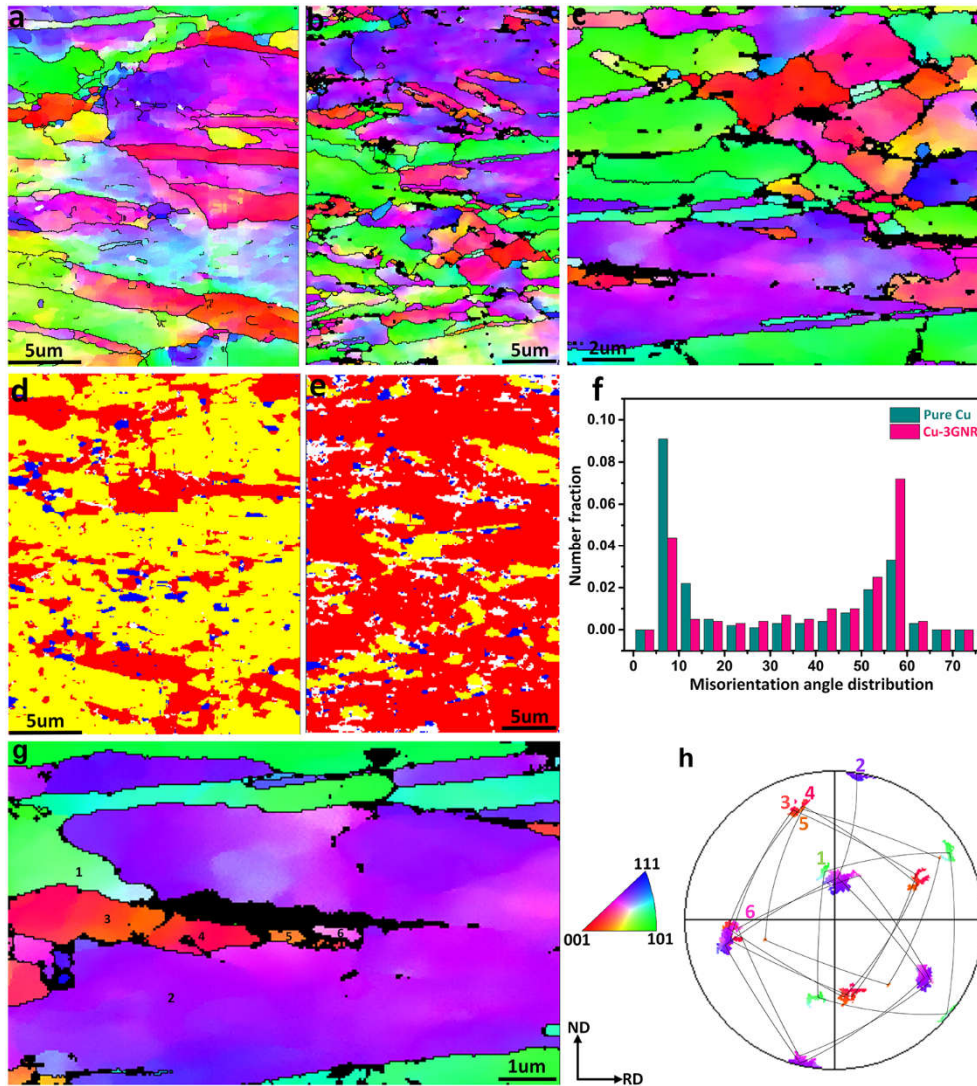


Fig. 5. IPF maps of (a) pure Cu and (b-c) 3GNR/Cu. The black areas indicating the GNRs. (d-e) Deformed (red), recovered (yellow), and recrystallized (blue) areas corresponding to (a-b), respectively. (f) Distribution of GB misorientation angles derived from (a-b). An obviously larger proportion of HAGBs is detected in 3GNR/Cu than that in pure Cu. (g) High-resolution EBSD showing the GNR-stimulated RX nucleation. (h) (100) pole figure of the orientations of 6 GNR-stimulation recrystallized grains labelled in (g).

Due to the very large deformation rate, the incubation duration is not sufficient for transforming the recovered grains into fully recrystallized grains. Thus, no obvious

recrystallized zone is found in GNRs/Cu. Within 0.5GNR/Cu and 1GNR/Cu, the β -fiber components are largely eliminated along with the increase of Goss component. Since the Goss orientation represents a conventional RX texture component, the promotion of RX process by the GCIs can well explain the enhancement of Goss component in 0.5GNR/Cu and 1GNR/Cu. The trade-off of β -fiber has been explained using the “ReNuc” model of RX whereby nucleation is deemed to occur on HAGBs between the β -fiber components of the lamellar bands in conjunction with orientation-dependent recovery [37]. In contrast, despite of the elevated rolling temperature, the rolling texture (β -fiber) is not significantly altered in pure Cu because the deformation rate is as high as 30 S^{-1} here and thus the extent of RX is weak. PF orientation analysis proves that the RX nucleation and growth in the GAZ follow an essentially random orientation manner (Fig. 5g-h), which resembles that in the PAZ [6, 24]. Therefore, the higher extent of DRX is, the lower intensity of final overall texture is evolved, as detected in GNRs/Cu.

Deformed, recovered, and recrystallized areas can further be distinguished from each other by analyzing local or in-grain orientation gradients. For this purpose we use the Kernel average misorientation (KAM) maps of the gradient GAZs under inspection [24, 38]. Fully recovered areas appear in such mappings as zones that are essentially free of local misorientations. In contrast, heavily deformed areas in the microstructure typically reveal high values of the local misorientation. The KAM is not necessarily homogeneously distributed but rather shows a characteristic pattern. This applies particularly in the vicinity of the GNRs, and the concentrated KAM near GNRs may also verify the dislocation pile-up in the GAZ (Fig. 6a-b) [24, 38]. In contrast, GNR-free area with relatively low KAM values are essentially free of local misorientations. The KAM distribution in pure Cu is relatively homogeneous (Fig. 6c-d).

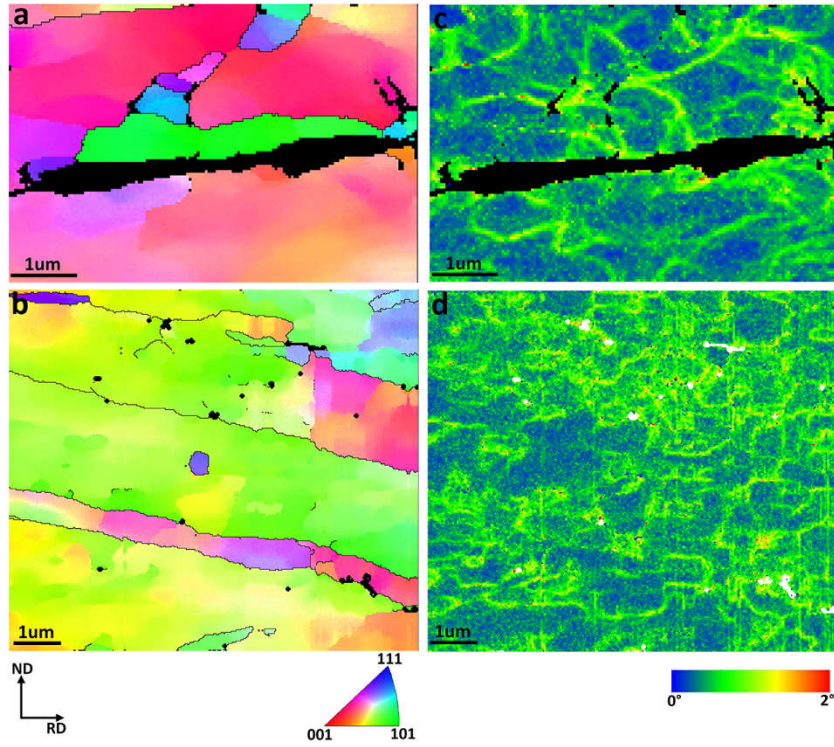


Fig. 6. (a-b) IPFs of pure Cu and GNRs/Cu. (c-d) KAM maps corresponding to (a-b), respectively.

TEM characterization (**Fig. 7a-c**) reveals that: i) the sizes of GAZs range from several hundred nanometers to 1–2 micrometers; ii) preferential nucleation of dislocation cells, subgrains, and DRX grains occur in the GAZ; and iii) dislocation is stacked near the GCIs. We then correlate the change of dislocation density, RX nucleation, and KAM distribution with the insertion of GCIs. During deformation, GNRs restrain the gilding, migration, and propagation of dislocations, and the dislocation pile-up can provide abundant recovery energy. For DRX nucleation, critical dislocation density refers to the dislocation needed to form large enough subgrains with sufficient surrounding stored energy to overcome the opposing pressure from boundary curvature. The acceleration of dynamic recovery and DRX results from the additional GNDs induced by the GCIs. The density of GNDs (ρ_{GND}) can be estimated by [12, 33]:

$$\rho_{GND} = \frac{8V_{GNR}\varepsilon_y}{b\gamma_s} + \frac{12V_{GNR}\Delta CTE \Delta T}{b(1-V_{GNR})\gamma_s} \quad (1)$$

where γ_s is the effective reinforcement particle diameter, V_{GNR} is the volume fraction, ε_y is the yielding strain, ΔCTE is the CTE mismatch between GNRs and Cu, and ΔT is the maximum temperature change during thermomechanical processing. The total dislocation density (ρ) variation with the distance from the GNRs (x) can also be estimated with respect to the misorientation angle (Θ) [1]:

$$\rho = \frac{K}{b} \frac{\Theta}{x} \quad (2)$$

With the absolute orientation gradient, the dislocation density is [1]:

$$\rho = \frac{c_1 \tan \Theta_{max} \cos^2 \Theta}{br} \left(-\frac{c_1 x}{2r} \right) \quad (3)$$

where c_1 and K are constants, b is the Burgers vector, Θ_{max} is a function of the shear strain, and r is the particle radius. The linear relationship between ρ and x is corroborated by HRTEM analysis (**Fig. 7d-f**), which shows a high density of dislocations generated in the very vicinity of the GCIs whereas the density drops sharply at a distance of < 20 nm from the interface. All these prove that the inhomogeneity of KAM in the GAZs and GNR-free areas and the stimulation of DRX both arise from the dislocation pinning effect. The evolution of RX-type texture is a result of the dynamic competition between the dislocation accumulation induced by the GCIs and the dislocation removal due to DRX.

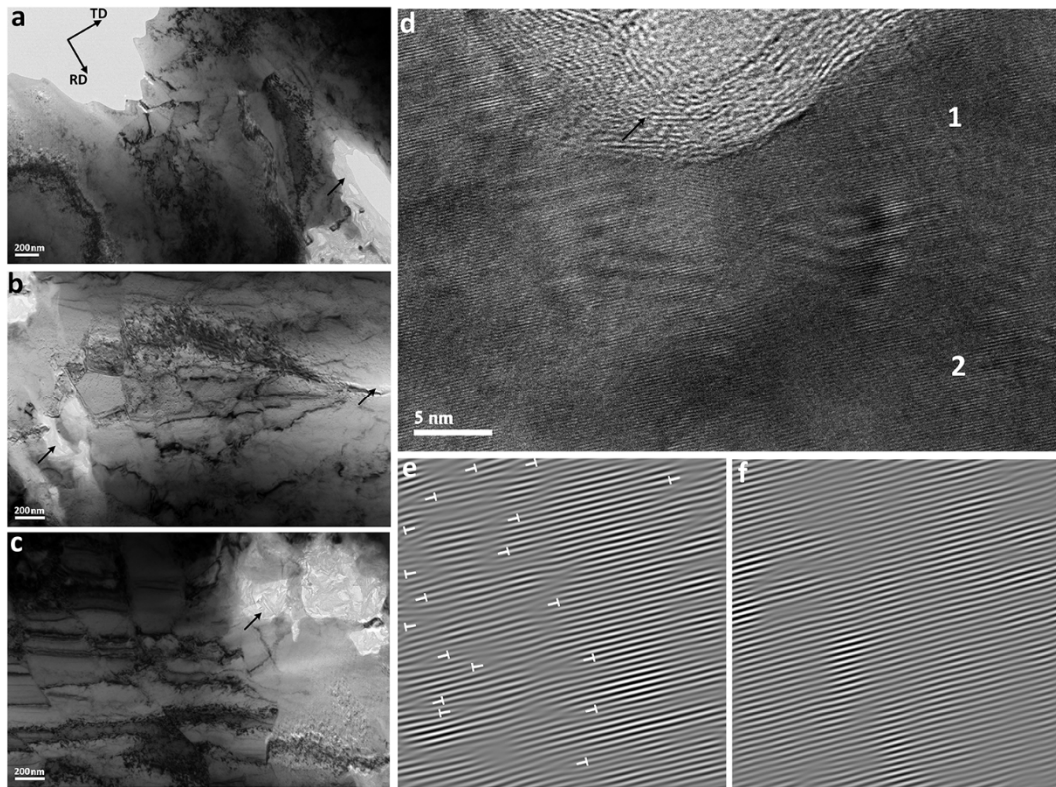


Fig. 7. (a-c) TEM images showing the microstructure, dislocation cells, subgrains, and DRX grains in the GAZ. GNRs are indicated by black arrows. (d) HRTEM image of the GCI region. (e-f) Inverse FFT images corresponding to regions 1 and 2 in (d), respectively. Dislocations are marked by “T”.

It is noteworthy that the P component, which is frequently observed in recrystallized Al alloys containing SPPs [7, 25, 34, 39], is not developed in GNRs/Cu. The evolution of the P component in recrystallized materials is related to the well-known particle stimulated nucleation mechanism and rationalized by the strain energy release maximization theory [7, 39]. The evolution of P-type textures can be explained by a model which combines both oriented nucleation and rapid growth of grains with a $40^\circ/\langle 111 \rangle$ orientation relationship to its surroundings. This concept rests on the idea that $40^\circ/\langle 111 \rangle$ grains have a growth advantage due to a higher mobility of the reaction front than growing grains of random orientations [4, 5,

25]. The P orientation has a $31.1^\circ/\langle 122 \rangle$ orientation relationship with respect to the Cube orientation, which is close to the $40^\circ/\langle 111 \rangle$ condition [40]. Finite element simulations have demonstrated that the strain field in the vicinity of non-deformable particles strongly deviates from the macroscopic one, which is responsible for the specific P-type texture in the PAZ during RX [5, 39].

PAZs may provide preferred RX nucleation sites, and the development of P orientations in such sites is substantially tied to the shape, size, and strain distribution of the PAZ [5, 41]. Although GNRs also induce a GAZ, the characteristics of micro-texture and microstructure in the vicinity of GAZ are rather different from that of a large constituent particle in traditional alloys [6, 34, 36]. This refers to a nano-scale effect due to the special quasi-1D geometry and atomic-level thickness of GNRs. As supported by the SEM (Fig. 1a-d), EBSD (Fig. 1i-j), and TEM (Fig. 7) results, no shear-band, obvious local deformation zone, or local lattice rotation is generated in GNRs/Cu; and the GAZs have sub-micrometer size. Therefore, the magnitudes of local strain and misorientation gradient are too small to trigger the specific P component. The distinction between GAZ and PAZ may rationalize why particle stimulated nucleation followed by an oriented growth of P-oriented grains, which is a commonly accepted premise in industrial grade Al alloys containing coarse non-deformable particles [5, 39], is not observed in our GNRs/Cu samples. It is also notable that the coarse particles in conventional alloys have little effect on the overall deformation texture when the volume fraction is relatively low (*e.g.* < 5%) [1]. GNRs in this study can significantly influence the texture evolution of the composites, which is also owing to their nano-size effect and large specific surface area (*i.e.*, interfacial area).

3.4 Non-octahedral slip

Correlating the addition of GCIs to the enhanced DRX extent can well explain the strengthening of Goss component at relatively low GNR fractions (*e.g.*, 0.5–1 vol.%). However, this correlation alone cannot rationalize why the anomalous brass-type texture is developed in 3GNR/Cu.

In FCC crystals, the usual operating slip is (111)<110>. It is well established that rolling deformation through the (111)<110> slip in FCC metals or alloys leads to the development of Cu, S, and Bs texture components [20]. The balance between Cu and Bs components is mainly determined by the value of SFE in these metals or alloys. The development of the Cu-type texture can be explained by Taylor-type models with straight-forward (111)<110> slip. As to the development of brass-type texture, a general agreement in relative theories is still lacking [3, 26]. Deformation twinning and shear-band theory are frequently adopted to explain the development of brass-type texture in Cu alloys (with relatively low SFE) and Cu-based dual-phase composites [42]. However, neither twinning nor shear band is particularly identified in GNRs/Cu here. Therefore, we conjecture that the brass-type texture evolution in 3GNR/Cu is likely to result from the dislocation-related factors only. Some studies have documented that brass-type textures may be the result of the predominance of non-octahedral (or non-compact) slip (*e.g.* (111)<112> slip) [26, 28-30]. Non-compact slip could occur extensively under conditions of nanocrystalline [43] or ultrafine-grained [28] materials, multiple slip [44], high strains and strain rates, and elevated rolling temperatures ($> 0.6 T_m$) [29, 30]. At higher strain rates, grain interactions become more important; multiple slip systems are activated and their interactions become more complex. At high temperatures, the critical resolved shear stress

(CRSS) for non-basal slip decreases dramatically [45].

In FCC materials perfect dislocations with $\frac{a}{2}[110]$ Burgers vector may dissociate into two Shockley partial dislocations with $\frac{a}{6}[211]$ Burgers vectors, for instance, $\frac{a}{2}[110] \rightarrow \frac{a}{6}[211] + \frac{a}{6}[12\bar{1}]$. These partial dislocations may slip thus introducing a new slip mode, $(111)\langle 112 \rangle$. It is well recognized that, for pure metals, the extent of partial diminishes with the SFE increasing [26]. Therefore, in normal conditions, pure Cu deforms by straight-forward $(111)\langle 110 \rangle$ slip due to its medium SFE, and dislocation partials are unlikely to form. Interestingly, it has been verified that, in the case of Cu-graphene composites, Shockley partials are initiated due to the pinning of full dislocations by the GCIs. It is possible that as with the inclusion of stiff graphene interfaces, there is a transition in the mechanism of slip from glide of perfect $\langle 110 \rangle$ dislocations to glide of uncoordinated slip by $\langle 112 \rangle$ Shockley partials [31]. This trend is presumably enhanced with the GNR fraction increasing (*i.e.*, the volume of GCIs).

In these regards, we propose that the second factor for the atypical texture evolution of GNRs/Cu is the activation of non-compact $(111)\langle 112 \rangle$ slip system, which is additional to the normal $(111)\langle 110 \rangle$ slip. Dislocation climb and cross slip are hindered by the GCIs, especially due to the high deformation temperatures, high strain rate, and large specific interfacial area of GNRs applied in this study. The increase of Bs component on one hand and the expense of Cu component on the other hand reflect that GNRs may stimulate non-octahedral slip in Cu in addition to the normal $\langle 110 \rangle$ cross slip. It is noteworthy that an individual GNR can cross several grains rather than residing at the grain boundaries [12]. This substantially enhances the interaction between the GCI and dislocations and may lead to a considerable high density of $\langle 112 \rangle$ partials. As revealed by the TEM images (Fig. 8a-b), a great deal of dislocation partials

are formed around the GCIs. HRTEM and FFT images (**Fig. 8c-f**) show intimate bonding between the Cu and GNR lattices at the atomic level. A robust interfacial bonding is prerequisite for effective interaction between the GCIs and dislocations. Moreover, strongly localized slip on only a few preferred slip systems will take place due to the nano-size effect of the GNRs, robust interfacial coherency, prominent GNDs storing at the GCIs to accommodate the strain incompatibilities, and the strong constraints to dislocation movement.

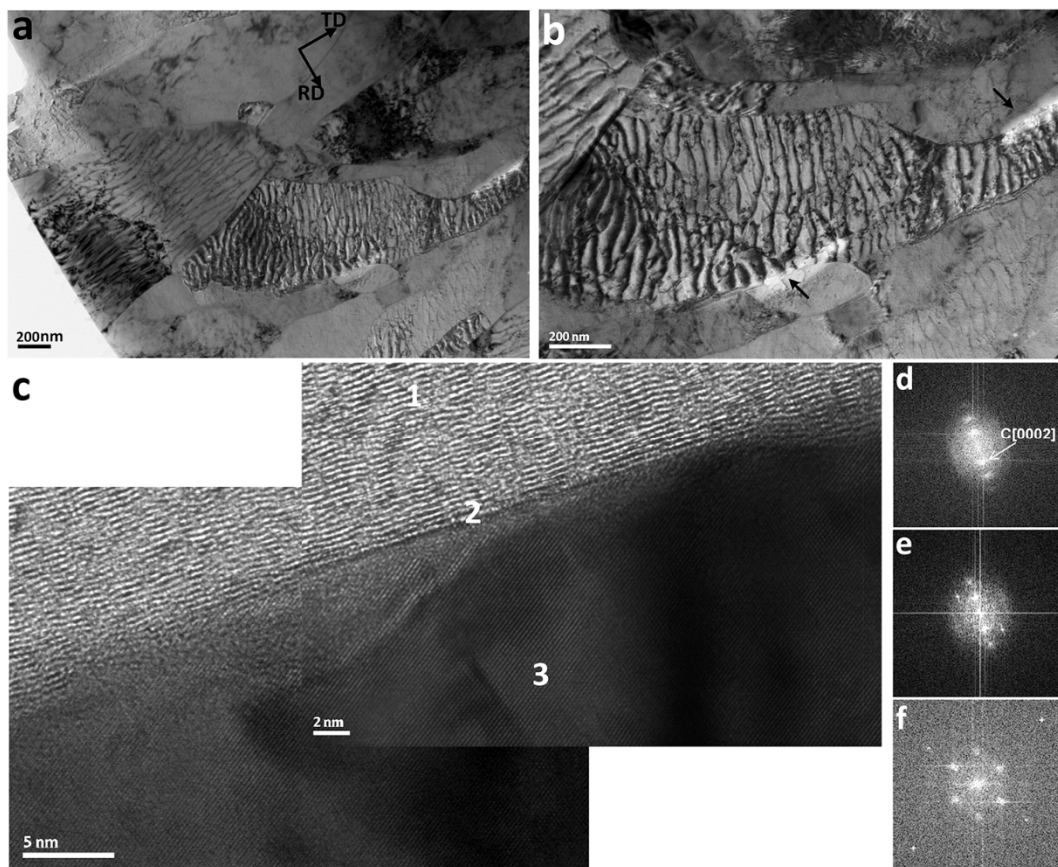


Fig. 8. (a-b) TEM images showing the Shockley partials. (c) HRTEM image revealing closely bonded GCIs. (d-f) FFT patterns corresponding to the lattices of Cu, GCIs, and GNRs (regions 1-3) in (a), respectively.

Within GNRs/Cu the stimulating effect of GCIs on the RX behavior operates along with their impact on the slip mode. Therefore, the appearance of brass-type texture in 3GNR/Cu instead of an increase strength of RX component observed in 0.5GNR/Cu indicates that, at

higher GNR fractions, the pinning effect of GCIs and the ensuing activation of additional slip system play a more predominant role in the texture evolution. For 1GNR/Cu, the texture transformation is dominated by the competition between the RX process and slip mode change, and thus the final texture is a balance of RX- (Goss) and Bs components.

3.5 VPSC simulation

The previous experimental studies indicate that the GCIs may heavily impact the texture evolution *via* accelerating the DRX process and changing the dislocation behavior and slip mode. The rise of Goss component within 0.5GNR/Cu suggests a promotion of dynamic recovery and DRX processes by the GCIs. The development of a (110)<112> brass-type texture instead of a (112)<111> Cu-type texture in 3GNR/Cu justifies that the normal cross-slip is suppressed due to the insertion of GCIs. The texture evolution in 1GNR/Cu follows a balance of RX-type and brass-type textures. To explore the roles of GNRs, we further implement VPSC polycrystal simulations to: i) provide an understanding on the texture development of metal-nanocarbon composites in hot-rolling process; ii) evaluate the roles of the GCIs in altering the DRX behavior and slip patterns of the matrix material; and iii) investigate how these changes influence the bulk texture evolution. In VPSC modelling, a single grain is treated as an ellipsoidal visco-plastic inclusion embedded in and interacting with an anisotropic homogeneous effective medium that corresponds to the polycrystalline aggregate [20, 27, 44]. The response of individual grains is described by the activation of various deformation systems (*s*) at predetermined values of the CRSS [45, 46]. The VPSC model has been proved to be successful in predicting texture evolution in both single-phase (*e.g.*, Cu [47], Ag [20], Mg [45], and Zr [46]) and multi-phase composites (*e.g.*, Cu-Nb [19], Cu-Ag [20], and Pt-Au [43]) under

load conditions involving large plastic straining and strain path changes.

The parameters that can be varied in VPSC are the polycrystal model itself and the assumed operating slip systems. Accordingly, the effects of GCIs can be investigated in the VPSC simulation by tuning the interaction coefficient, the CRSS value and the CRSS ratio of possible slip systems, and the coupling coefficient. **Table 1** lists the parameters for VPSC simulation considering the different operating slip systems and polycrystal models (*i.e.*, interaction coefficient) between pure Cu and GNRs/Cu. These parameters are assigned by taking into account the effects of GCIs on the DRX process, dislocation interaction (*i.e.*, confinement, annihilation, or initiation), and slip mode, as discussed previously in Section 3.2-3.4.

Table 1. Constitutive parameters for VPSC simulations of pure Cu and GNRs/Cu.

GNR fraction	Slip system	τ_0	τ_1	θ_0	θ_1	$h^{ss'}$	n^{eff}
0	(111)<110>	33.5	1200	100	5	1.4	1
0.5	(111)<110>	12.5	1200	100	5	1.1	1/10
	(111)<112>	19	1200	100	5	1.1	
1	(111)<110>	33.5	1200	100	5	1	1/20
	(111)<112>	25	1200	100	5	1	
3	(111)<110>	40.5	1200	100	5	1	1/20
	(111)<112>	33.5	1200	100	5	1	

The variation in the polycrystal model is possible by changing a single parameter—the so-called interaction coefficient α in the interaction equation of the VPSC model, which relates the grain-level stress (s^g) and strain rate (d^g) to the aggregate counterparts (S, D) [27]:

$$s^g - S = n^{eff}(\Gamma^{sgg^{-1}} + A^s)(d^g - D) \quad (4)$$

For example, $n^{eff} = 0, 1, \infty$, and $1/m$ (m : strain-rate sensitivity parameter) correspond to modeling by the Sachs, Secant, Taylor, and Tangent polycrystal models, respectively [43, 47].

Previous modeling studies on FCC rolling texture have indicated that the transition from Cu- to brass-type texture is generally dictated by two main factors, *i.e.*, the grain-matrix interaction scheme and the inclusion or exclusion of deformation twinning [27]. When deformation twinning is not taken into account, the Taylor (upper)- and Sachs (lower)-type models lead to Cu- and brass-type rolling textures, respectively. Therefore, the interaction schemes can be adjustable to reflect the strength of the coupling between the stress and strain rate deviations. Considering the remarkable blocking effects of GNRs on dislocation sliding, as proven by the (HR)TEM characterizations (Figs. 7-8), we define an interaction coefficient $n^{eff} = 1/20$ for 1GNR/Cu and 3GNR/Cu, $n^{eff} = 1/10$ for 0.5GNR/Cu, and $n^{eff} = 1$ for pure Cu.

The VPSC model also involves the Voce hardening model as follows [27, 44]:

$$\tau^s(\Gamma) = \tau_0 + (\tau_1 + \theta_1\Gamma)[1 - \exp(-\Gamma \left| \frac{\theta_0}{\tau_1} \right|)] \quad (5)$$

where for each grain the accumulated strain is $\Gamma = \int_0^t \sum |\Delta\gamma^s| dt$; $\Delta\gamma^s$ is the shear rate on slip system s ; and τ_0 , τ_1 , θ_0 and θ_1 govern the hardening of s . The operating slip systems can be mediated by adjusting the CRSSs, *i.e.*, the parameters τ_0 , τ_1 , θ_0 , and θ_1 , of the corresponding systems.

In the case of GNRs/Cu, the effect of GNRs in terms of pinning down the dislocations, generating GNDs, and removing dislocations *via* accelerating dynamic recovery and DRX should be considered. Meanwhile, the dislocation density of each slip α is updated based on dislocation generation (plasticity) and removal (recovery and RX) [45, 46]:

$$\frac{\partial \rho^\alpha}{\partial \gamma^\alpha} = k_1^\alpha \sqrt{\rho^\alpha} - k_2^\alpha(T, \dot{\epsilon}) \rho^\alpha \quad (6)$$

Parameter k_2^α is temperature (T) and strain rate ($\dot{\epsilon}$) dependent:

$$\frac{k_2^\alpha(T, \dot{\epsilon})}{k_1^\alpha} = \frac{b^\alpha \chi}{g^\alpha} \left(1 - \frac{KT}{D^\alpha b^3} \ln\left(\frac{\dot{\epsilon}}{\dot{\epsilon}_0}\right) \right) \quad (7)$$

where γ^α is the shear strain; g^α , D^α , $\dot{\epsilon}_0$, and k_1^α are the hardening parameters of slip α .

The forest hardening of slip α is calculated by [45]:

$$\tau_{forest}^\alpha = b^\alpha \chi u \sqrt{\rho^\alpha + \rho_{GND}} \quad (8)$$

where χ is the hardening parameter and u is the shear modulus. The VPSC model also allows for the possibility of “self” and “latent” hardening by defining coupling coefficient $h^{ss'}$, which empirically accounts for the obstacles that new dislocations associated with s' activity represent for the propagation of system s .

$$\Delta\tau^s = \frac{d\tau^s(\Gamma)}{d\Gamma} \sum_{s'} h^{ss'} \Delta\gamma^{s'} \quad (9)$$

where $\Delta\tau^s$ represents the increase in the CRSS of slip system s by slip shearing on other systems s' . Thus, the updated CRSS of slip α (herein, (111)<110> and (111)<112> slip systems) can be expressed as:

$$\tau_{CRSS}^\alpha = \tau_0^\alpha + \tau_{forest}^\alpha + \Delta\tau^s \quad (10)$$

Qualitatively, the CRSS for normal cross slip is heavily increased due to the additional dislocation within the GAZ. Thereby the activation of additional <112> partial slip is possible to accommodate overall dislocation movement, and this possibility is in proportion to the volume fraction of GCIs. Accordingly, the effect of GCIs can be expressed in the VPSC simulation by tuning the CRSS value and the CRSS ratio of (111)<112> and (111)<110> slip [26]. The Voce parameters are assigned primarily according to previous studies [19, 20]. Within 0.5GNR/Cu, the dislocation removal *via* recovery and RX dominates, thus τ_0 is set to a relatively low value (see Table 1). In contrast, as revealed by our previous study [12], the accumulated dislocation density in 3GNR/Cu at $\epsilon = 1.94$ is nearly 8 times larger than that in the pure Cu counterpart. Therefore, $\tau_0^{<110>}$ for 3GNR/Cu is set to 40.5 MPa as compared to

33.5 MPa for pure Cu.

As shown in **Fig. 9**, the corresponding PFs and ODF figures obtained from the simulation results agree well with the experimental observations (Figs. 2-4). Specifically, for pure Cu, we find that the development of classical Cu-type texture is best simulated with the Taylor model taking (111)<110> octahedral slip exclusively, which is consistent well with previous studies [26, 28, 47]. As to GNRs/Cu, a reasonable fit can be produced *via* the selection of specific <110> and <112> slip systems, polycrystal model, and coupling coefficient. For 0.5GNR/Cu, we make available to $\tau_0^{<110>}/\tau_0^{<112>} = 1:1.5$, yielding 95% and 5% slip activity, respectively [43]. The stimulation effect of GNRs on the DRX process can be reflected by reducing the values of $h^{ss'}$ and α . For 1GNR/Cu, we assign to <112> slip the same Voce parameters as <110> slip but with $\tau_0^{<110>}/\tau_0^{<112>} = 1.34:1$ to enforce a predominance of <112> slip [20]. For 3GNR/Cu, the predominance of Bs component and its deviation from the ideal position are best simulated with the Tangent model by assuming the dominant slip of $1/6<112>$ partial dislocations on (111) planes and weak interaction between the grains, respectively (see Table 1).

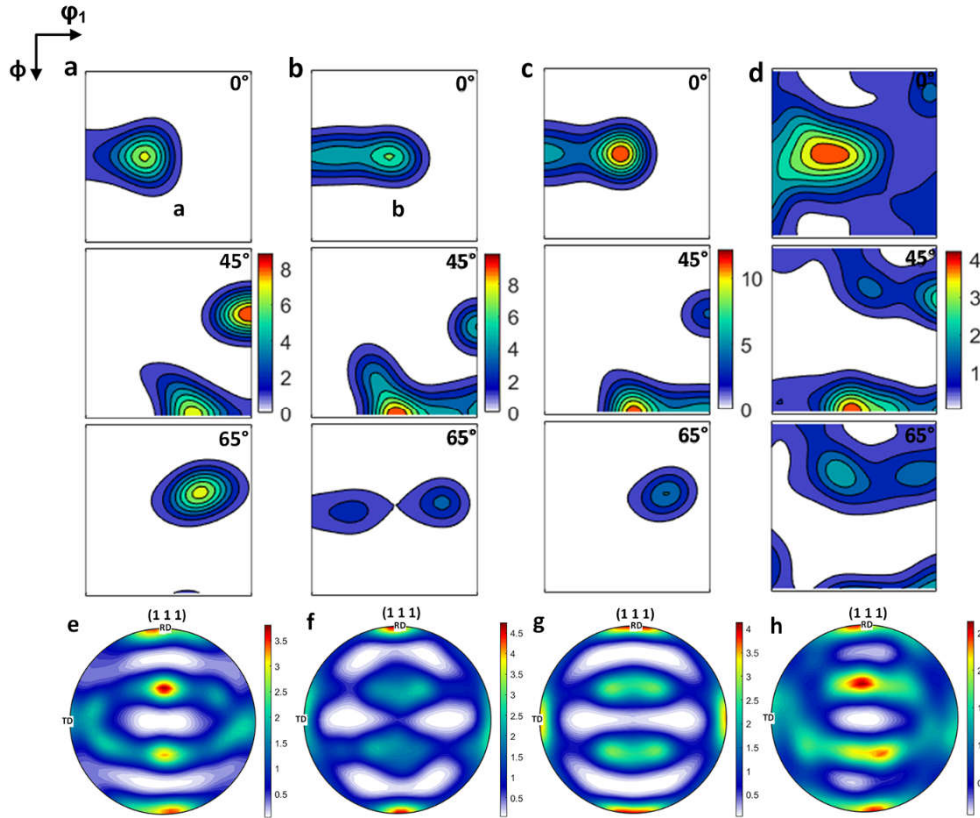


Fig. 9. (a-d) ODF representations at $\varphi_2 = 0^\circ, 45^\circ,$ and 60° obtained from the VPSC simulation results of pure Cu, 0.5GNR/Cu, 1GNR/Cu, and 3GNR/Cu, respectively. (e-h) (111) PFs corresponding to (a-d), respectively.

The consistency between the experimental and simulated texture data further confirms the roles of the GCIs on the DRX and texture evolution of bulk composites. It is clear from the modeling that texture evolution in GNRs/Cu is dependent on non-compact slip in addition to conventional $111\langle 110 \rangle$ slip. Qualitative and quantitative analyses of the calculated textures indicate that texture evolution in the Cu phase is significantly influenced by the GCIs, which either promotes partial dislocations or acts as a barrier to slip (or possibly both). Furthermore, it is noteworthy that texture measurement for composites containing > 3 vol.% GNRs is not implemented in this study because of the obvious aggregation of GNRs in the Cu matrix at

such high fractions. Nevertheless, it can be speculated from the simulation results that, for Cu-based composites with higher volume fractions, a more predominantly brass-type texture will develop. This can be ascribed to more obvious changes of the dislocation-GCI interaction and the operating slip mode with amounts of GNRs increasing, despite higher extents of dynamic recovery and DRX are also expected.

4. Conclusions

To summarize, we demonstrate interface-directed DRX behavior and texture evolution in a GNR-reinforced Cu matrix composite. Macro- and micro-texture measurements show an increased strength of Goss component in 0.5GNR/Cu, a brass-type texture in 3GNR/Cu, and a balance of Goss and Bs component in 1GNR/Cu, which deviate from the normal Cu-type texture forming in the pure Cu counterpart. TEM, HRTEM, EBSD, and KAM analyses prove that the GCIs may influence the deformation behavior of the Cu matrix from the following four aspects: i) retarding dislocation cross slip and piling up dislocations; ii) generating GNDs; iii) promoting DRX nucleation; and vi) activating non-compact $\langle 112 \rangle$ slip. Furthermore, the deviations of the texture developed in 0.5GNR/Cu, 1GNR/Cu, and 3GNR/Cu are rationalized by the GNR-stimulating nucleation effect, and a balance of both, respectively. This is supported by VPSC simulations, which well reproduce the texture development in all samples by assigning the VPSC parameters considering the interface-dislocation interaction, GNR-stimulated DRX and activation of non-octahedral slip.

Interface-mediated DRX process and texture evolution as revealed by this study suggest the exciting possibilities of manipulating the microstructure, texture, and mechanical properties of traditional metallic materials through the design of heterophase interfaces. It is suggested that,

other low-dimensional materials (*e.g.*, CNTs and BN nanoribbon) may function well as GNRs on altering the deformation behavior of the matrix phase. Hetero-interfaces prepared by top-down methods (*e.g.*, powder blending in this study) instead of bottom-up methods (*e.g.*, precipitation in traditional alloys) may offer high flexibilities for engineering the properties of the interfaces, *e.g.*, the size, geometry, orientation, spatial distribution, fraction, and bonding strength. Moreover, further exploration of the relation between metal-nanofiller interfaces is important for potential applications because the hot-rolling processing adopted here is much close to the industrial conditions.

References

- [1] K. Huang, K. Marthinsen, Q. Zhao, R.E. Logé, The double-edge effect of second-phase particles on the recrystallization behaviour and associated mechanical properties of metallic materials, *Prog Mater Sci* 92 (2018) 284-359.
- [2] J. Hirsch, T. Al-Samman, Superior light metals by texture engineering: Optimized aluminum and magnesium alloys for automotive applications, *Acta Mater* 61(3) (2013) 818-843.
- [3] T. Leffers, R.K. Ray, The brass-type texture and its deviation from the copper-type texture, *Prog Mater Sci* 54(3) (2009) 351-396.
- [4] J.J. Sidor, R.H. Petrov, L.A.I. Kestens, Modeling the crystallographic texture changes in aluminum alloys during recrystallization, *Acta Mater* 59(14) (2011) 5735-5748.
- [5] J.J. Sidor, K. Decroos, R.H. Petrov, L.A.I. Kestens, Evolution of recrystallization textures in particle containing Al alloys after various rolling reductions: Experimental study and modeling, *Int J Plasticity* 66 (2015) 119-137.
- [6] R.P. de Siqueira, H.R.Z. Sandim, D. Raabe, Particle Stimulated Nucleation in Coarse-Grained Ferritic Stainless Steel, *Metall Mater Trans A* 44(1) (2012) 469-478.
- [7] K. Huang, K. Zhang, K. Marthinsen, R.E. Logé, Controlling grain structure and texture in Al-Mn from the competition between precipitation and recrystallization, *Acta Mater* 141 (2017) 360-373.
- [8] Y. Wang, J. Aktaa, Microstructure and texture in W and W-1wt%La₂O₃ processed by high-pressure torsion, *Scripta Mater* 139 (2017) 22-25.
- [9] S.C. Tjong, Recent progress in the development and properties of novel metal matrix nanocomposites reinforced with carbon nanotubes and graphene nanosheets, *Mater Sci Eng R* 74(10) (2013) 281-350.
- [10] A. Nieto, A. Bisht, D. Lahiri, C. Zhang, A. Agarwal, Graphene reinforced metal and ceramic matrix composites: a review, *Int Mater Rev* 62(5) (2016) 241-302.
- [11] F. Mokdad, D.L. Chen, Z.Y. Liu, B.L. Xiao, D.R. Ni, Z.Y. Ma, Deformation and

- strengthening mechanisms of a carbon nanotube reinforced aluminum composite, *Carbon* 104 (2016) 64-77.
- [12] M. Yang, L. Weng, H. Zhu, T. Fan, D. Zhang, Simultaneously enhancing the strength, ductility and conductivity of copper matrix composites with graphene nanoribbons, *Carbon* 118 (2017) 250-260.
- [13] J. Hwang, T. Yoon, S.H. Jin, J. Lee, T.S. Kim, S.H. Hong, S. Jeon, Enhanced mechanical properties of graphene/copper nanocomposites using a molecular-level mixing process, *Adv Mater* 25(46) (2013) 6724-9.
- [14] J. Wang, Z. Li, G. Fan, H. Pan, Z. Chen, D. Zhang, Reinforcement with graphene nanosheets in aluminum matrix composites, *Scripta Mater* 66(8) (2012) 594-597.
- [15] Q.-h. Yuan, G.-h. Zhou, L. Liao, Y. Liu, L. Luo, Interfacial structure in AZ91 alloy composites reinforced by graphene nanosheets, *Carbon* 127 (2018) 177-186.
- [16] S. Feng, Q. Guo, Z. Li, G. Fan, Z. Li, D.-B. Xiong, Y. Su, Z. Tan, J. Zhang, D. Zhang, Strengthening and toughening mechanisms in graphene-Al nanolaminated composite micro-pillars, *Acta Mater* 125 (2017) 98-108.
- [17] Z. Li, Q. Guo, Z. Li, G. Fan, D.B. Xiong, Y. Su, J. Zhang, D. Zhang, Enhanced Mechanical Properties of Graphene (Reduced Graphene Oxide)/Aluminum Composites with a Bioinspired Nanolaminated Structure, *Nano Lett* 15(12) (2015) 8077-83.
- [18] M. Yang, L. Weng, H. Zhu, F. Zhang, T. Fan, D. Zhang, Leaf-like carbon nanotube-graphene nanoribbon hybrid reinforcements for enhanced load transfer in copper matrix composites, *Scripta Mater* 138 (2017) 17-21.
- [19] J.S. Carpenter, S.C. Vogel, J.E. LeDonne, D.L. Hammon, I.J. Beyerlein, N.A. Mara, Bulk texture evolution of Cu–Nb nanolamellar composites during accumulative roll bonding, *Acta Mater* 60(4) (2012) 1576-1586.
- [20] I.J. Beyerlein, N.A. Mara, D. Bhattacharyya, D.J. Alexander, C.T. Necker, Texture evolution via combined slip and deformation twinning in rolled silver–copper cast eutectic nanocomposite, *Int J Plasticity* 27(1) (2011) 121-146.
- [21] I.J. Beyerlein, M.J. Demkowicz, A. Misra, B.P. Uberuaga, Defect-interface interactions, *Prog Mater Sci* 74 (2015) 125-210.
- [22] S. Cho, K. Kikuchi, A. Kawasaki, On the role of amorphous intergranular and interfacial layers in the thermal conductivity of a multi-walled carbon nanotube–copper matrix composite, *Acta Mater* 60(2) (2012) 726-736.
- [23] M. Yang, L. Hu, X. Tang, H. Zhang, H. Zhu, T. Fan, D. Zhang, Longitudinal splitting versus sequential unzipping of thick-walled carbon nanotubes: Towards controllable synthesis of high-quality graphitic nanoribbons, *Carbon* 110 (2016) 480-489.
- [24] J. Konrad, S. Zaefferer, D. Raabe, Investigation of orientation gradients around a hard Laves particle in a warm-rolled Fe₃Al-based alloy using a 3D EBSD-FIB technique, *Acta Mater* 54(5) (2006) 1369-1380.
- [25] Q. Zhao, K. Huang, Y. Li, K. Marthinsen, Orientation Preference of Recrystallization in Supersaturated Aluminum Alloys Influenced by Concurrent Precipitation, *Metall Mater Trans A* 47(3) (2016) 1378-1388.
- [26] K. Wierzbanski, M. Wroński, T. Leffers, FCC Rolling Textures Reviewed in the Light of Quantitative Comparisons between Simulated and Experimental Textures, *Crit Rev Solid State Mater Sci* 39(6) (2014) 391-422.

- [27] A.A. Saleh, C. Haase, E.V. Pereloma, D.A. Molodov, A.A. Gazder, On the evolution and modelling of brass-type texture in cold-rolled twinning-induced plasticity steel, *Acta Mater* 70 (2014) 259-271.
- [28] C.F. Gu, L.S. Toth, Y.D. Zhang, M. Hoffman, Unexpected brass-type texture in rolling of ultrafine-grained copper, *Scripta Mater* 92 (2014) 51-54.
- [29] C. Maurice, J.H. Driver, Hot rolling textures of f.c.c. metals—Part I. Experimental results on Al single and polycrystals, *Acta Mater* 45(11) (1997) 4627-4638.
- [30] C. Maurice, J.H. Driver, Hot rolling textures of f.c.c. metals—Part II. Numerical simulations, *Acta Mater* 45(11) (1997) 4639-4649.
- [31] Y. Kim, J. Lee, M.S. Yeom, J.W. Shin, H. Kim, Y. Cui, J.W. Kysar, J. Hone, Y. Jung, S. Jeon, S.M. Han, Strengthening effect of single-atomic-layer graphene in metal-graphene nanolayered composites, *Nat Commun* 4 (2013) 2114.
- [32] I.J. Beyerlein, N.A. Mara, J. Wang, J.S. Carpenter, S.J. Zheng, W.Z. Han, R.F. Zhang, K. Kang, T. Nizolek, T.M. Pollock, Structure–Property–Functionality of Bimetal Interfaces, *JOM* 64(10) (2012) 1192-1207.
- [33] L. Jiang, H. Yang, J.K. Yee, X. Mo, T. Topping, E.J. Lavernia, J.M. Schoenung, Toughening of aluminum matrix nanocomposites via spatial arrays of boron carbide spherical nanoparticles, *Acta Mater* 103 (2016) 128-140.
- [34] S. Tangen, K. Sjølstad, T. Furu, E. Nes, Effect of Concurrent Precipitation on Recrystallization and Evolution of the P-Texture Component in a Commercial Al-Mn Alloy, *Metall Mater Trans A* 41(11) (2010) 2970-2983.
- [35] J.D. Robson, D.T. Henry, B. Davis, Particle effects on recrystallization in magnesium–manganese alloys: Particle-stimulated nucleation, *Acta Mater* 57(9) (2009) 2739-2747.
- [36] H. Jazaeri, F.J. Humphreys, The transition from discontinuous to continuous recrystallization in some aluminium alloys, *Acta Mater* 52(11) (2004) 3239-3250.
- [37] M.Z. Quadir, O. Al-Buhamad, L. Bassman, M. Ferry, Development of a recovered/recrystallized multilayered microstructure in Al alloys by accumulative roll bonding, *Acta Mater* 55(16) (2007) 5438-5448.
- [38] M. Calcagnotto, D. Ponge, E. Demir, D. Raabe, Orientation gradients and geometrically necessary dislocations in ultrafine grained dual-phase steels studied by 2D and 3D EBSD, *Mater Sci Eng A* 527(10-11) (2010) 2738-2746.
- [39] J. Jung, J.I. Yoon, D.N. Lee, H.S. Kim, Numerical analysis on the formation of P-orientation near coarse precipitates in FCC crystals during recrystallization, *Acta Mater* 131 (2017) 363-372.
- [40] Q. Zeng, X. Wen, T. Zhai, Effect of Precipitates on the Development of P Orientation {011} <566> in a Recrystallized Continuous Cast AA 3004 Aluminum Alloy after Cold Rolling, *Metall Mater Trans A* 40(10) (2009) 2488-2497.
- [41] C. Schäfer, J. Song, G. Gottstein, Modeling of texture evolution in the deformation zone of second-phase particles, *Acta Mater* 57(4) (2009) 1026-1034.
- [42] N. Jia, D. Raabe, X. Zhao, Texture and microstructure evolution during non-crystallographic shear banding in a plane strain compressed Cu–Ag metal matrix composite, *Acta Mater* 76 (2014) 238-251.
- [43] W. Skrotzki, A. Eschke, B. Jóni, T. Ungár, L.S. Tóth, Y. Ivanisenko, L. Kurmanaeva, New experimental insight into the mechanisms of nanoplasticity, *Acta Mater* 61(19) (2013) 7271-

7284.

[44] A.A. Saleh, E.V. Pereloma, A.A. Gazder, Microstructure and texture evolution in a twinning-induced-plasticity steel during uniaxial tension, *Acta Mater* 61(7) (2013) 2671-2691.

[45] Q. Ma, B. Li, W.R. Whittington, A.L. Oppedal, P.T. Wang, M.F. Horstemeyer, Texture evolution during dynamic recrystallization in a magnesium alloy at 450°C, *Acta Mater* 67 (2014) 102-115.

[46] I.J. Beyerlein, C.N. Tomé, A dislocation-based constitutive law for pure Zr including temperature effects, *Int J Plasticity* 24(5) (2008) 867-895.

[47] C.F. Gu, M. Hoffman, L.S. Toth, Y.D. Zhang, Grain size dependent texture evolution in severely rolled pure copper, *Mater Charact* 101 (2015) 180-188.